Soft X-ray Fermi surface tomography of palladium and rhodium via momentum microscopy

Xin Liang Tan [a,*], Kenta Hagiwara [a], Ying-Jiun Chen [a,b], Jakub Schusser [c,d], Iulia Cojocariu [a,e], Daniel Baranowski [a], Vitaliy Feyer [a], Ján Minár [c], Claus M. Schneider [a,b,f], Christian Tusche [a,b]

[a] Peter Grünberg Institut (PGI-6), Forschungszentrum Jülich, 52425, Jülich, Germany
[b] Fakultät für Physik, Universität Duisburg–Essen, 47057, Duisburg, Germany
[c] New Technologies Research Centre, University of West Bohemia, 30614, Pilsen, Czech Republic
[d] Experimentelle Physik VII and Würzburg-Dresden Cluster of Excellence ct.qmat, Universität Würzburg, 97074, Würzburg, Germany
[e] Elettra - Sincrotrone Trieste S.C.p.A., S.S. 14 - km 163.5, 34149, Basovizza, Trieste, Italy
[f] Department of Physics, University of California Davis, One Shields Ave., 95616 CA, Davis, USA

ARTICLE INFO

ABSTRACT

Fermi surfaces of transition metals, which describe all thermodynamical and transport quantities of solids, often fail to be modeled by one-electron mean-field theory due to strong correlations among the valence electrons. In addition, relativistic spin–orbit coupling pronounced in heavier elements lifts the degeneracy of the energy bands and further modifies the Fermi surface. Palladium and rhodium, two 4d metals attributed to show significant spin–orbit coupling and electron correlations, are ideal for a systematic and fundamental study of the two fundamental physical phenomena and their interplay in the electronic structure. In this study, we explored the Fermi surface of the 4d noble metals palladium and rhodium obtained via high-resolution constant initial state momentum microscopy. The complete 3D-Fermi surfaces of palladium and rhodium were tomographically mapped using soft X-ray photon energies from 34 eV up to 660 eV. To fully capture the orbital angular momentum of states across the Fermi surface, the Fermi surface tomography was performed using p- and s-polarized light. Applicability and limitations of the nearly-free electron final state model in photoemission are discussed using a complex band structure model supported by experimental evidence. The significance of spin–orbit coupling and electron correlations across the Fermi surfaces will be discussed within the context of the photoemission results. State-of-the-art fully relativistic Korringa–Kohn–Rostoker (KKR) calculations within the one-step model of photoemission are used to support the experimental results.

1. Introduction

The introduction of geometry into the modern electron theory of metals has revolutionized the description of the electronic structure of metals from the idea of a degenerate Fermi gas into Fermi surfaces. The Fermi surface topology of a solid describes all of its transport properties as the Fermi surface corresponds to the momentum-resolved boundary between the occupied and unoccupied states. By the early 1970s, the Fermi surfaces of metallic systems were studied intensively using density functional theory. Experimental confirmations of the Fermi surface topology were primarily performed using De Haas–van Alphen oscillations [1–3]. Fermi surfaces allow us to understand the electronic interactions such as Ruderman–Kittel–Kasuya–Yosida interaction and inter-layer exchange coupling in thin films, which subsequently led to the discovery and fundamental description of giant magnetoresistance [4,5]. However, Fermi surfaces of solids with higher

valency and strong correlations may deviate significantly from the free electron-like electronic structure. Describing fine structures in an intricate Fermi surface topology has proven to be challenging from both experimental and theoretical points of view. Recent developments in electron spectroscopy have proven momentum-resolved photoelectron spectroscopy to be the preferred technique to investigate electronic structures and Fermi surface topology owing to its unprecedented energy and momentum resolution [6,7]. In this study, we will explore the three-dimensional high-resolution Fermi surface tomography of single-crystal elemental 4d transition metals palladium (Pd) and rhodium (Rh) via state-of-the-art electron spectroscopy in the form of momentum microscopy.

Photoelectron spectroscopy, despite being a staple probe for electronic structures, is inherently an indirect technique in which the

---
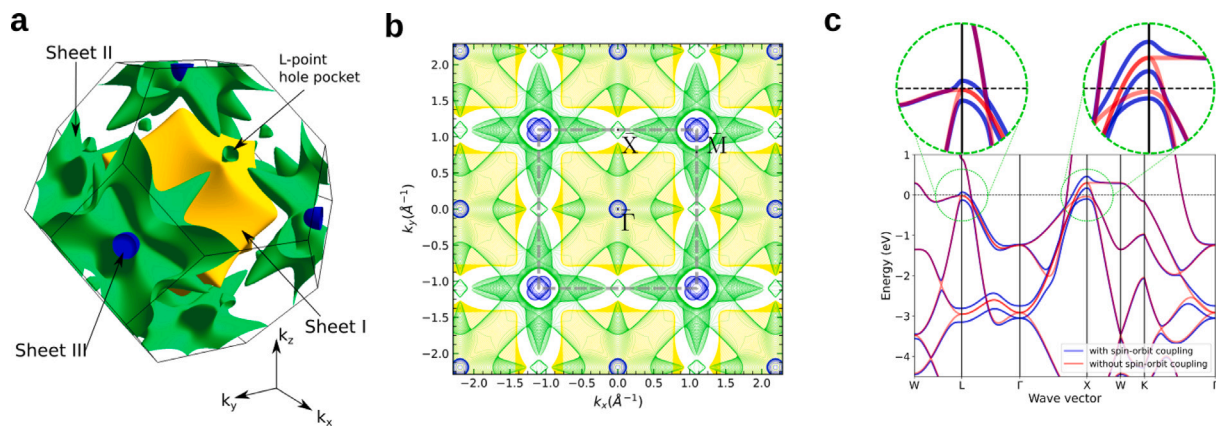
Fig. 1. **a** Relativistic Fermi surface of Pd calculated using FPLAPW with LDA+U formalism. **b** Projection of the Fermi surface contours of the LDA+U ground state in k_z dimension. The surface Brillouin zone convention is used for consistency where the dashed line denotes the surface Brillouin zone boundary. **c** Comparison between the ground state calculations with and without consideration of spin–orbit coupling. The insets (2.5× magnification) highlight the significance of the relativistic effect on the Fermi surface of Pd.

experimental observable, the photoelectron spectral function is a convolution of the initial ground state and final excited state of the crystal with respect to a defined electromagnetic field. Pioneering theoretical efforts [7–11] have established the fundamental framework for the photoemission process and interpretations of the experimental observation. However, due to a multitude of experimental parameters and the setup limitation, the photoemission models are mostly used as a qualitative link between the experimental observation and the theoretical description of the physical interactions. Although conventional photoelectron spectroscopic techniques, such as angle-resolved photoemission spectroscopy (ARPES) allow access to the electronic structure with high energy and momentum resolutions, it is fundamentally limited by geometrical confinements of its photoelectron acceptance angle and momentum resolution [6]. The two-dimensional mapping of the electronic structure using a photoelectron emission microscope was first demonstrated two decades ago [12], and further developed by combining the microscopy with a hemispherical deflection analyzer for unprecedented momentum and energy resolutions also known as momentum microscopy [6,13–17]. By using momentum microscopy with an energy-variable light source, we are able to eliminate the physical constraints and the redundant parameters in conventional photoemission experiments. Our findings have allowed us to explore the fine structures in photoemission spectra, for instance, the complete highly resolved Fermi surface and the anomalies observed at lower photon energies.

In this study, the complete three-dimensional Fermi surfaces of palladium (Pd) and rhodium (Rh) are resolved experimentally and theoretically. Complementary to our experimental results, fully relativistic Korringa–Kohn–Rostoker (KKR) calculations within the one-step model of photoemission were employed for discussion of the experimental spectral features [10,18]. Furthermore, the momentum-resolved photoemission process is revisited using fundamental textbook examples of wave functions in a periodic lattice potential [19] and the application of a one-step photoemission process.

Elemental Pd is commonly treated as the model case study for ferromagnetic instability in an itinerant electronic system. As a 4d-elements with electron configuration [Kr] $4d^{10}$, Pd is iso-electronic to the ferromagnetic element nickel (Ni). In its ground state, despite possessing a high density of states at the Fermi energy, elemental Pd narrowly fails to fulfill the Stoner criterion for ferromagnetic order. Hence, it is conventionally classified as a nearly-ferromagnetic metal. The (para) magnetic susceptibility of Pd is a result of the system being on the verge of ferromagnetic transition [20]. The strong magnetic fluctuation and the anomalous temperature variation of the enhanced paramagnetic susceptibility of Pd were studied intensively via a spin fluctuation model [21]. Over the past decades, various studies have

shown that ferromagnetism in Pd can be achieved via dimensionality reduction or quantum well state formation in ultrathin Pd films. Moreover, a neighboring 3d-ferromagnet in epitaxially strained Pd film or multilayer configurations can easily spin-polarize a near-ferromagnet like Pd. Elemental Pd is also predicted to have a magnetic onset upon lattice expansion of less than 5% [22].

Neighboring Pd in the periodic table, Rh has one less valency with electron configuration [Kr] $5s^1 4d^8$. The electronic structure of rhodium has not been studied extensively [23]. However, the recent discovery of topological chiral charges in RhSi [24] and the coexistence of spin and charge ordering on monolayer Fe on Rh(001) [25] have motivated further understanding of its electronic structure. In addition, both Pd and Rh are staples in compounds engineered to host non-collinear spin textures. A complete description of the electronic structure of elemental Pd and Rh is crucial to provide a convincing ansatz to their physical properties and their potential application in future technology. Here, we provide some insights into the roles of strong spin–orbit coupling and correlations played in the electron structure of Rh and Pd, especially across their Fermi surface.

2. Fermi surface of palladium

In order to establish a fundamental framework, the ground state of face-centered cubic Pd, shown in Fig. 1 is calculated using an all-electron full-potential linearized augmented-plane wave (FPLAPW) code [26] ($U = 1.0$ eV, $J = 0.3$ eV) with spin–orbit coupling included in second variation [27]. k-point mesh sizes of $15 \times 15 \times 15$ was used and the Fermi surface was plotted onto a $100 \times 100 \times 100$ grid. A total of 70 empty states are used to ensure convergence for the unoccupied bands.

The Fermi surface of Pd in Fig. 1a can be classified into three separate Fermi sheets or bands. Sheet I (yellow) primarily exhibits a free electron-like character and manifests as a deformed sphere in the zone center at Γ-point with spikes pointing towards L- and X- high-symmetry points in the zone boundary; Sheet II (green) contributes the most to the density of states in the vicinity of Fermi energy. It manifests as interconnected hollow tubes between the X points of the Brillouin zone, commonly called "jungle gym", with horn-like features pointing away from X-point towards the L-point. With the inclusion of spin–orbit coupling in the theoretical calculations, as shown in Fig. 1c, a small hole pocket at the L-point is realized; Sheet III (blue) exists as elliptical hole pockets around X points. The radius of the hole pocket is also strongly modified following the inclusion of spin–orbit coupling. The Fermi level was set by direct comparison of the radii of Sheet II contours between theoretical and experimental data in the latter sections. Despite consistent with previous literature [27–29], the
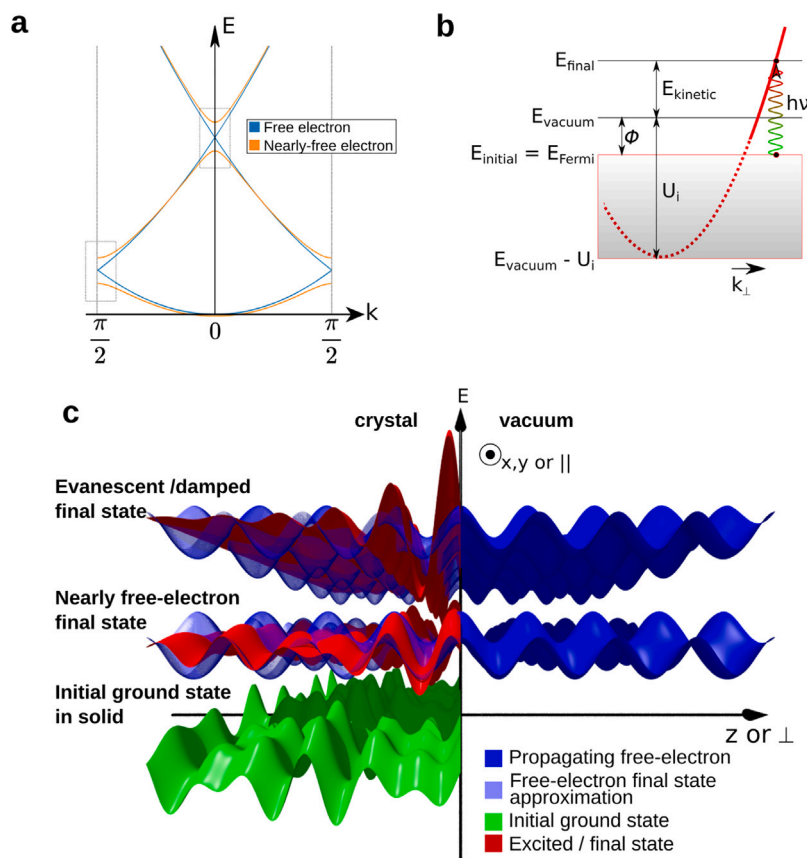
Fig. 2. a Comparison between empty lattice-free electron dispersion and nearly-free electron dispersion with periodic lattice potential. **b** The energy diagram of free electron final state of photoelectron for the satisfaction of wave matching condition. **c** Illustration of the wave-matching conditions in real space for excitation into a damped final state and an available unoccupied final state. Note the mismatch in the out-of-plane component $k_\perp$ of an evanescent wave with the free electron wavefunction.

Fermi energy of both X and L hole pockets is evidently overestimated in FPLAPW when compared to the experimental data. Consequently, the radii of hole pockets appear significantly smaller than expected. Fig. 1**b** shows the Fermi surface contours in k_x and k_y with respect to defined k_z values. These contours are composed of 100 equally divided cross-sections of a complete Brillouin zone of Pd.

3. Experimental methods

The momentum microscopy experiments were carried out at the NanoESCA beamline of the Elettra synchrotron in Trieste, Italy, using photons in the energy range between 35 eV and 660 eV with variable polarization. Photoelectrons emitted into a complete half-sphere of 2π sr solid angle above the crystal surface were collected by an electrostatic immersion lens and mapped onto a valence band spectral intensity distribution of lateral momenta (k_x, k_y) of the crystal. Meanwhile, the perpendicular momentum $k_\perp$ is not conserved due to the breaking of translational symmetry at the sample surface. The sample remained stationary throughout the experiments. Hence the three primary variables are photon energy, photon polarization, and the selected photoelectron energy. In all measurements, the lateral momentum resolution $\Delta k_\parallel$ of the momentum microscope is better than 0.02 Å^{-1}. The overall energy resolutions ΔE are better than 50 meV and 100 meV for photon energy below and above 200 eV, respectively. All experimental results, unless otherwise mentioned, are raw photo-electron intensity maps without any additional image processing or symmetrization, except for the mandatory flat field correction of the multichannel plate detector.

Photoemission processes in the low energy regime represent a complex issue and the photoemission final state plays an important role

in the overall spectral function, as can be seen in Refs. [30,31]. Our study can be classified into two separate energy regimes based on photon energies applied, low energy (34 eV–200 eV) and high energy regime (>200 eV). Here, in the high-energy limit, we adopted the interpretation of the free electron final state model where convergence to the free-electron final state is ensured. Fig. 2**a** shows the textbook example of a free electron dispersion and a more realistic dispersion with a periodic potential. In this model, the ground state wave function within the crystal (initial state) is excited into a free electron-like final state which is perfectly matched to a free electron dispersion in the vacuum, as shown in the solid line in Fig. 2**b**. In a particle across a step well picture in Fig. 2**c**, the wave-matching condition between blue-colored and red-colored wave functions across the surface (step) has to be satisfied. The simplicity of the free electron model permits the extraction of the out-of-plane wave vector, $k_\perp$ under the assumption of constant crystal inner potential. The kinetic energy of the measured photoelectrons is selected in conjunction to the varied photon energy, hence keeping the probed initial state constant. The final states are represented by plane wave approximation as a free electron-like iso-energy sphere in momentum space cutting across the Brillouin zone. Its radius is given by $|\mathbf{k}| = \frac{\sqrt{2m}}{\hbar}\sqrt{E_{\text{kinetic}} + U_i}$, where the inner potential, U_i, can be generalized as a material-dependent quantity.

In our microscopy results, the lateral wave vectors (k_x, k_x) are kept constant along with the momentum resolution. Therefore, the sample size of photoelectrons decreases as a function of the reduced solid angle of emission in real space while cutting across the iso-energy spherical surface of constant solid angle in momentum space at higher energies, resulting in lower photoelectron transmission. For instance, in the case of Pd, the acquisition time of the Fermi surface at a photon energy of 55 eV was 30 seconds, whereas a similar experiment at a photon energy

of 620 eV took 1200 seconds or 20 minutes. In addition, the beamline photon flux also follows a downward trend with increasing photon energy [32], resulting in overall reduced photoelectron statistics in the high energy regime.

The angle of incidence of photons, as measured from the sample surface, was fixed at 25° as shown in Fig. 3**a** together with the $\vec{E}$ field vector we defined for p-polarization. The orthogonal linear polarization, s-polarization, is then defined by the condition in which the $\vec{E}$ field vector is in the plane with the x-axis (k_x) of Fig. 3**a**. Linear polarization is useful not only to determine the symmetry of observed states but also to simplify observable electronic bands by sorting out the orbital symmetry of the initial states based on the dipole selection rule [7]. Under the dipole approximation, the initial state can be categorized as even or odd with respect to the reflection in the mirror plane spanned by the Poynting vector of the incident photon and the direction of photoemission. The observable final state of photoemission must always be even as an odd parity will result in a node in the electron wave function. Therefore, the even-symmetry initial states are only observable in p-polarization, whereas the odd-symmetry initial states are only observable in s-polarization [33]. As a side note, we would like to mention that a prior study on the Fermi surface of Pd [34] using linear polarizations failed to address some of the key features in its theoretical Fermi surface, such as Sheet III and the hole pocket of Sheet II.

The elemental single-crystals of Pd(001) and Rh(001) were cleaned in situ by repeated cycles of Ar-ion sputtering and annealing at 850 K in an ultra-high vacuum consistently below 1×10^{-9} mbar for 10mins. The sample surface is re-prepared every four hours to ensure a pristine surface. All measurements were performed with the sample temperature at 130 K.

4. Fermi surface tomography

For the Pd(001) and Rh(001) single-crystals, we determined values of U_i = 19.25 eV and 16.50 eV respectively, by comparing a series of constant initial state momentum maps with that of the calculated ground states as shown in Fig. 1. Supplementary materials 1 and 2 show the respective videos of the constant-initial state momentum microscopy scan at Fermi energy overlaid with the zone boundary under the free-electron final state model with the determined U_i. Figs. 3**b** and **c** show the spherical cuts with the X-point of the Brillouin zone at the origin while Figs. 3**d** and **e** feature that of Γ- high symmetry points. The general consistency between the Fermi surface topology of the third zone and the fourth zone is remarkable. All the theoretical features are well reproduced in the experimental results with small deviations from the FPLAPW results, as mentioned in the previous subsection.

However, the limitations of the free electron final state model can already be seen in the momentum map obtained at 246 eV photon energy in Fig. 3**b**. As pointed out by the two small arrows with dark blue outlines, signatures of the horn-like feature of Sheet II in the vicinity of the projected $\bar{X}$-point could be seen at around $(k_x, k_y) = (0, \pm1.15)$ and $(\pm1.15, 0)$. In order to make a case for discussions on such an anomaly of the photoemission spectral response at lower photon energies, we employed constant initial state momentum microscopy tomographically by scanning across photon energies in fine intervals to access a larger energy–momentum phase space.

Owing to the aforementioned increase in photoelectron sampling size in the low energy regime, constant initial state momentum maps were obtained with energy intervals of 2 eV in photon energy. Detailed three-dimensional spectral responses in the momentum space of k_x and k_y as a function of photon energies are obtained. Fig. 4**a** presents the starting point for a curious case of spectral intensity modulations along the "jungle-gym" bands at 148 eV excitation energy which might be misinterpreted as part of the ground state of Pd. Adopting a similar convention in Figs. 3, 4**b**,**c** and **d** are overlaid with the respective zone boundary of Brillouin zone across different initial states. An apparent

reduced spectral intensity can be directly correlated with the zone boundary in the final state.

In order to visualize the trend across the tomography, we present an extracted cut of the spectra along the k_x-axis in Fig. 4**a** as a function of photon energy. Then, we overlaid the bulk zone boundary (red) across the photon energy cuts across the measurements at Fermi energy in Fig. 5**a**. This observation can be traced back to the forbidden band gaps in nearly-free electronic bands due to the presence of a periodic lattice potential shown in Fig. 2**a**. In our findings, the lack of spectral intensity in our results can be associated with the band gap in the photoelectron final state.

The breakdown of the free electron final state model close to the zone boundary can be understood as the unavailability of a final state, and therefore the final state is strongly damped. Here, we can clearly see the breakdown of the free electron final state model in the measurements taken in the low energy regime. Although the Sheet III hole pocket is expected around the X-point of the bulk zone boundary between the photon energy of 70 eV and 90 eV, we did not observe a strong contribution from Sheet III. Surprisingly, strong photoemission spectral intensity with Sheet III signature was observed off X high symmetry point. We associated this observation as a final state damping due to surface barrier potential and adopted the convention of the complex band structure in photoemission to capture these anomalies.

5. Complex band structure

Thus far, we have explored the electronic structure of Pd based on an infinite crystalline solid which can be understood as stationary Bloch waves made up of an ensemble of real energy eigenvalues. However, in the presence of a surface barrier potential, a complex-valued wave vector is adopted and the amplitude of the corresponding wave functions expands or decays exponentially along the out-of-plane ($\perp$) direction, resulting in the formation of evanescent states [35] as shown in Fig. 2**c**. As a consequence, the $k_\perp$ of the photoelectron becomes ill-defined by the free electron-like dispersion or even the bulk real states. Instead, one can interpret such states as final state self-energy or inelastic scattering of the photoelectron, which is known to limit the probing depth of photoemission. Hence, the momentum-resolved photoelectron spectral function has to satisfy the wave-matching condition for both the Bloch wave extending across the lattice and the evanescent states onto an incoming plane wave in vacuum, as shown in Fig. 2**c** [36,37]. Building upon a prior study on self-energy in an itinerant magnet [38], we demonstrated the evidence of final state self-energy in detail using constant-initial states momentum microscopy. Antithetically, in this study, the lifetime broadening due to the correlations of the initial state or the valence bands is strongly suppressed as the initial state is constrained to the Fermi level.

As evident in Fig. 5**a**, the free electron model deviates the most when the final state is situated close to the zone boundary. In order to describe our experimental observations in Fig. 5**a**, a calculation of the complex band structure based on the optical potential is performed, as shown in Fig. 5**b**. The transmission probability of photoelectrons or photocurrent in the normal emission photoemission geometry is plotted against the out-of-plane wave vector ($k_\perp$). A clear deviation of the observable real part of the complex band structure in blue and the bulk states in red can be seen at lower photon energies while slowly converging with increasing excitation or photoelectron energy. In particular, close to the zone boundary of X and Γ (back-folded), we can see dispersionless waterfall-like features, denoted as orange arrows in Fig. 5**b**, with respect to photo energy, suggesting heavy final state spatial damping. Drawing an analogue from Ref. [38], this can be understood as imaginary valued wave vectors driven by the complex final state self-energy particularly prominent close to the forbidden gap along the zone boundary.

The signature of the aforementioned Sheet III hole pocket visualized in the theoretical Fermi surface and our results obtained at higher
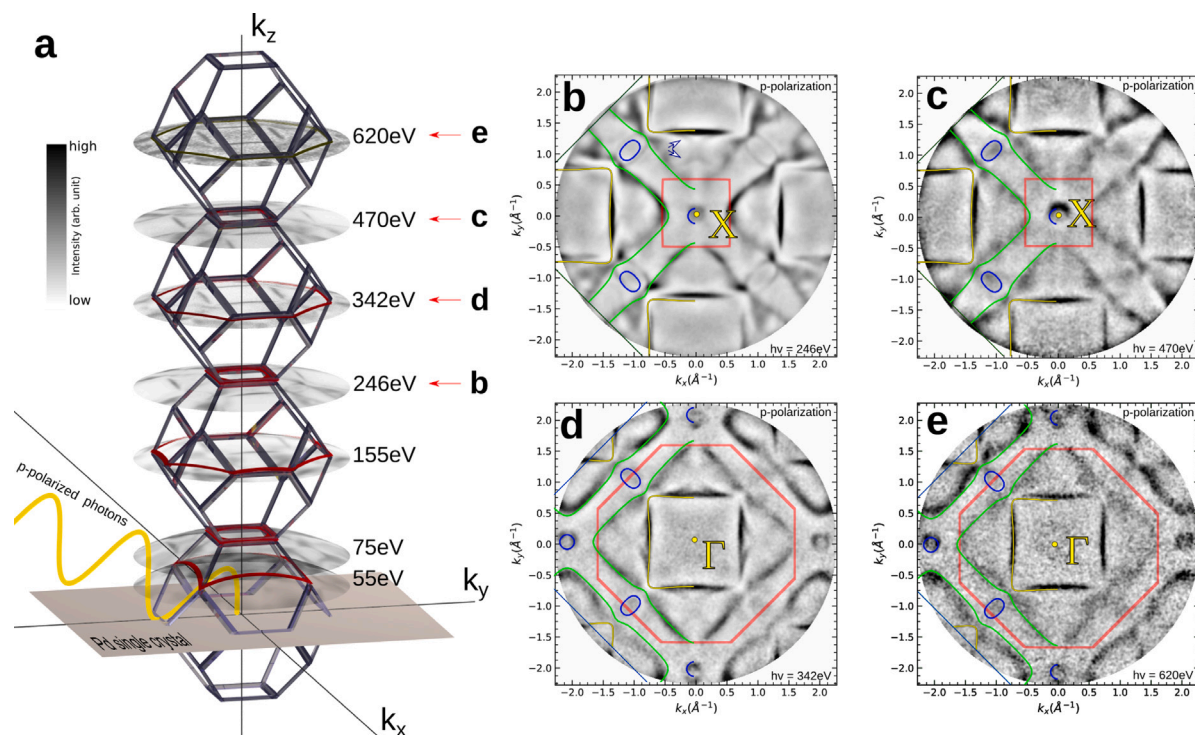
Fig. 3. a Experimental geometry and equi-energy free-electron final state spherical cuts in 3D momentum space corresponding to the experimental momentum maps. **b, c, d, e** show the experimental momentum maps at Fermi energy obtained at soft-X-ray energies of 246 eV, 470 eV, 342 eV, and 620 eV, respectively. Red overlay illustrates the intersections between the corresponding momentum disc and the first Brillouin zone boundary in the nearly-free electron final state model whereas the theoretical Fermi contour of palladium from local density approximation are overlaid on the left half of **b, c, d, e**.
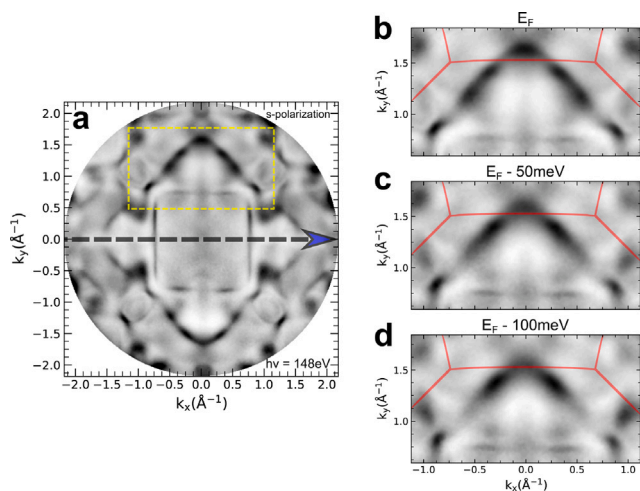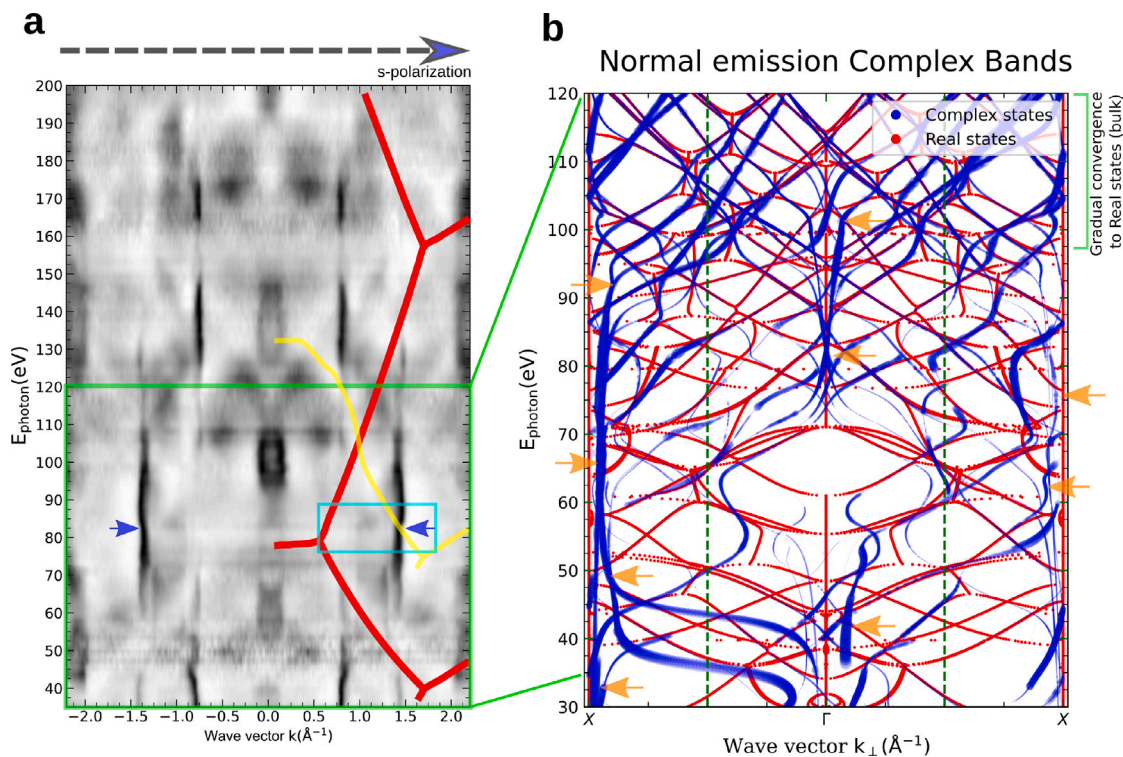

Fig. 4. a Momentum map taken with s-polarized photon of 148 eV. **b, c, d** Magnified constant momentum maps at Fermi energy, 50 meV and 100 meV below Fermi energy, respectively, in the region enclosed by a dashed yellow rectangle in **a**. Close to the zone boundary described by the free electron-like final state model, the photoelectron intensity is significantly reduced despite the change in the initial state.

energy regime in Fig. 3 is used as a pointer for comparison due to its defined feature and its position along normal emission (Γ - X). As mentioned in the previous section, the Sheet III hole pocket is displaced from its expected wave vector around the X-point of the bulk zone boundary in the vicinity of 75 eV photon energy. The strong signature of the Sheet III hole pocket in the experiment at around 105 eV can be associated with the eventual crossings at X in the calculation at the same energy. In addition, ghosting of the Sheet III hole pocket could

be seen at several energies where the real part of the complex band structure grazes/crosses the X-point.

Remarkably, we can also observe the momentum dependence of final state damping by tracing the regions with reduced photocurrent as we did with the bulk zone boundary. Due to the aforementioned complex surface barrier potential, the trace of the ghost zone boundaries adopts rather deformed dispersions, reflecting the waterfall-like dispersion in the real part of the normal emission complex band structure. We overlaid one of such dispersion of the zone boundary in a yellow solid line in Fig. 5a. The information on this effect is crucial as it may result in misinterpretation of ground state electronic structure in photoemission experiments. One such interesting observation is the appearance of kinks in bands of the constant initial state photoemission. Because of its strong photoelectron intensity and conspicuous feature, we selected the region marked by blue arrows in Fig. 5a, which is part of the relatively flat Sheet I. Fig. 6 shows the momentum map in the vicinity of the marked kinks. Experimentally we see the marked "ghost" duplicate of the zone boundary crossing the bands at around 84 eV photon energy where the kinks are observed. An abrupt and clear displacement orthogonal to the zone boundary of the Fermi Sheet I feature can be clearly seen in the spectra between Figs. 6c and d. An enlarged region of interest in dashed green squares is also shown in Fig. 6g and h where the wave vector is shifted in $+k_x$ direction. Away from the zone boundary, other spectral features evolve smoothly across different photon energies. One should not confuse the observation of such final state quasi-particles with those of the ground state as this phenomenon is primarily a consequence of the momentum-conserved photoemission process.

To provide a holistic picture, the momentum-resolved photoelectron spectral response of Palladium is evaluated theoretically using a one-step photoemission formalism. Local spin density approximation (LSDA) and atomic-spheres approximation (ASA) were used in the one-step model of photoemission calculations implemented in the SPR-KKR band structure software package [10]. A lattice constant of 7.3507 a.u. was used in the calculation.

Fig. 5. a Cross-sections along the k_x axis (arrow in Fig. 4**a**) of the normalized constant initial state momentum maps at Fermi energy, taken with the s-polarized photon. The zone boundary of the free electron final state model is plotted in a red solid line on the right half. The yellow line highlights one of the doubles of the zone boundary marked by a significant lack of photoelectron intensity. The semi-transparent box in green highlights the energy range covered in **b** while the blue arrows denote the kink-like features in the dispersion. **b** The real part of the out-of-plane wave vector component of the complex photoemission band structure (in blue) and the real bulk ground states (in red) in the normal $((k_x, k_y) = (0,0))$ photoemission geometry with respect to the photon energies. The transmission probability (photocurrent) of the real part complex states is plotted as a function of line thickness in a logarithmic scale. Orange arrows positioned across the complex states highlight the waterfall-like dispersion close to high symmetry points.

Fig. 7 shows the direct comparisons of the momentum distribution of photoemission spectral intensities at selected photon energies, of which the nearly-free electron final state sphere cuts across the L-, X-, and Γ- high symmetry points of Pd crystal at photon 55 eV, 75 eV, and 155 eV respectively. Each set of momentum maps at the selected photon energies, obtained in both p- and s- polarized photons, conforms well to its respective one-step photoemission calculation.

Strong suppression of the photoelectron intensity in the vicinity of zone boundary around $(k_x, k_y) = (\pm 0.5, \pm 0.5)$ in Figs. 7**c, d** due to the heavy final state damping, were reproduced in both experiments and theory. At 55eV photon energy, the L-hole pocket is clearly resolved in Fig. 7**a** but vanishes in Fig. 7**b**. Here, we are able to clearly resolve the hitherto unconfirmed small L-point hole pocket of Sheet II in Fig. 7**a**. We associate the polarization-dependent observation with the even- and odd symmetry of the orbital angular momentum of the states. Furthermore, we can also see the orbital selective photoemission of Sheet I along the $\Gamma - K$ high symmetry line in Fig. 7**e** and **f**. The yellow pointer in the figure shows a vanishing photoemission intensity along the $\Gamma - K$ direction only when s-polarized photons are used. Specifically, this band features a strong $d_{x^2-y^2}$ character (even-symmetry) of which the photo-excitation is forbidden in s-polarization.

In Fig. 7**a-d**, two concentric, hallowed but orthogonal ellipses (blue arrow) of Sheet III hole pocket centered at X- points of Brillouin zone (see Fig. 1**b**). Supplementary material 1 shows the Fermi surface tomography of Pd in the low energy regime where the two ellipses appear almost dispersionless across photon energies below 150 eV. It also emphasizes the vicinity of the ellipses with respect to the zone boundary. Similarly, this can be associated with the bulk zone boundary at $(k_x, k_y) = (\pm 1.15, \pm 1.15)$ or the $\bar{M}$-point of surface Brillouin

zone. At this specific momentum, the final state is always located in the vicinity of a zone boundary (see the overlay in supplementary material 1). As a result, the final state self-energy dominates resulting in a near two-dimensional-like state, mirroring an extreme case of the elongated pocket of the same Fermi sheet in Fig. 5**a**. This is, however, as we understand now a consequence of the final state self-energy of photoemission and should not be taken as a piece of direct information from the bulk band structure nor a surface state.

On the other hand, along with this knowledge, we are able to qualitatively resolve parts of the orbital texture of the Sheet III hole pocket around the X-point. In Fig. 7**e** and **f**, the blue arrows denote the position of the Sheet III hole pocket taken at 155 eV excitation energy. Here we can already observe the top/bottom part in k_z of the hole pocket as smaller dark-filled ellipses using p-polarized photons, signifying an even orbital. Meanwhile, the s-polarized photons exclusively photoexcite the upper (blue arrow in Fig. 7**f**) and lower portion of the hallowed edge of the ellipse. However, a further theoretical study of the orbital-resolved band structure is required for a detailed study. In a nutshell, we demonstrated the use of polarization-dependent momentum microscopy and the consequences of final state self-energy in bulk band mapping.

6. Fermi surface of rhodium

Neighboring Pd in the periodic table, the electronic structure of Rh is complementary to that of Pd as it has one less valence electron while featuring a face-centered cubic lattice with a slightly smaller lattice constant. Parameters similar to that of Pd are used in the FPLAPW code [26] for the relativistic band structure. The Fermi surface of Rh, as
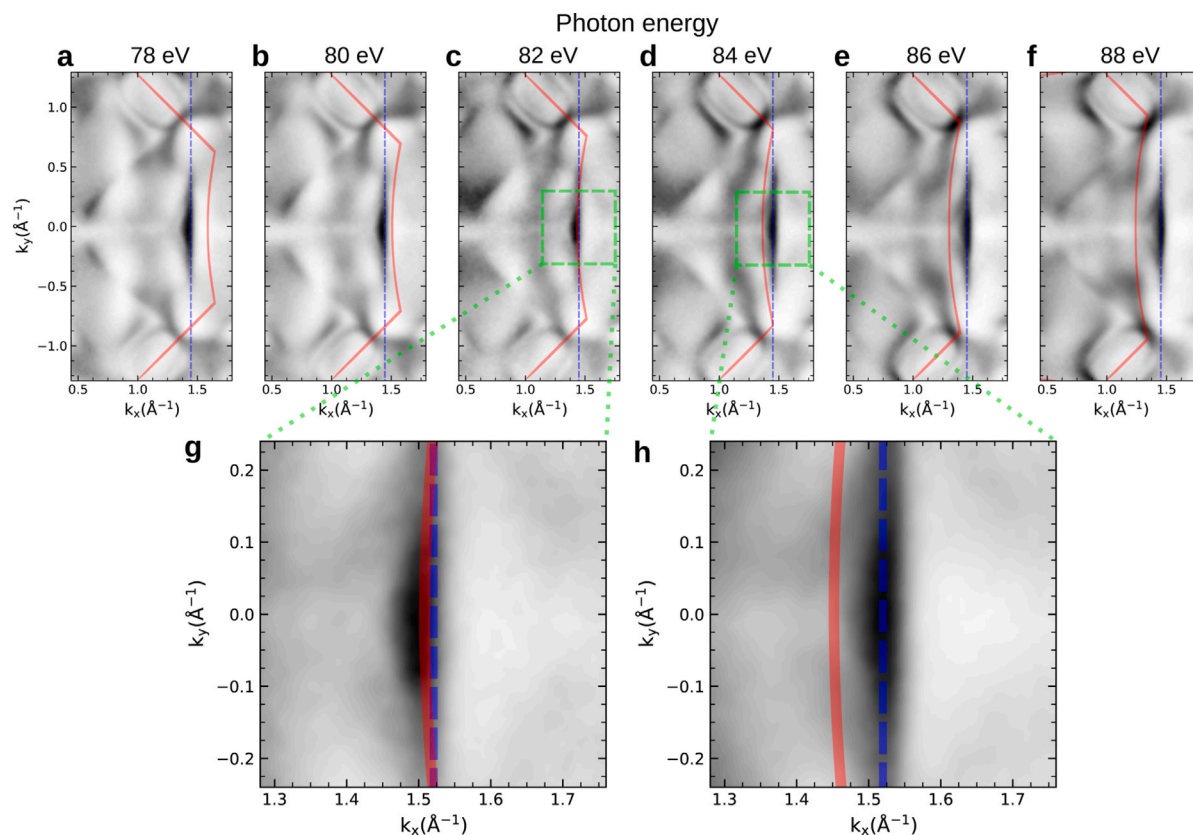
Fig. 6. Constant initial state momentum maps in the vicinity of zone boundary double formed in the existence of evanescent final state highlighted in a semi-transparent blue rectangular box in Fig. 5**a**. Translucent red and blue overlays are eye guides for the zone boundary and the anchor of k_x for visualization of the kink-like feature across the gap in the final state, respectively. **g,h** are the magnified momentum maps where the "kink"-like momentum displacement is most significant for 82 eV and 84 eV photon energies respectively, while the other bulk states evolve gradually.

shown in Figs. 8**a** and **b**, lacks the "jungle gym" Fermi surface topology of Pd. By comparing the respective band diagrams of Pd and Rh in Fig. 1**c** and Fig. 8**c**, we can see the similarity of two electronic structures with a shift in Fermi level due to the valence number. For the same reason, Rh has an extra Fermi sheet compared to Pd as an additional band crosses the Fermi energy. Such difference can be clearly seen with the band extrema of Pd situated below Fermi energy at L and X high symmetry point in Fig. 1**c**.

The Fermi surface of Rh can be categorized into four different Fermi sheets, as shown in Figs. 8**a** and **b**. Sheet A (orange) primarily exhibits a free electron-like character and manifests as a deformed sphere in the zone center at Γ-point with spikes pointing towards L- and X- high-symmetry points in the zone boundary. It is fully enclosed by Sheet B; Sheet B (green) manifests as a large Fermi sheet just short of electrons to form the "jungle gym" structure. It also protrudes towards the K high symmetry point and tucks closely between Sheet A and Sheet C. Sheet C (teal) exists as large deformed elliptical hole pockets around X-points with petal-like protrusion towards K-point. The radius of the hole pocket is also strongly modified following the inclusion of spin–orbit coupling. Similar to Pd, with the inclusion of spin–orbit coupling in the theoretical calculations, a small hole pocket at the L-point is realized; Sheet D (blue) appears as elliptical hole pockets around X-point enclosed by Sheet C. Consistent with Pd, the Fermi energy in theory was tuned to match with the d-like Sheet B in the experiment.

Based on our study on Pd, similar experimental pipelines were carried out to investigate the Fermi surface of Rh. A set of measurements between photon energies of 34 eV and 100 eV was carried out in 2 eV intervals and another set between photon energies of 500 and

652 eV was carried out. The aforementioned U_i of Rh is used in the free electron final state model. Fig. 9**a** shows the free electron final state cuts across the Brillouin zones for the selected momentum maps in Fig. 9**b-e**. Our interpretation on the complex final state model in the lower photon energy regime allowed us to understand the lack of spectral weight for the sheet C and sheet D hole pockets in Fig. 9**c**. Likewise, the deviation from the free electron final state model is significant in both Figs. 9**b** and **c** at photon energies of 60 eV and 79 eV, respectively. Remarkably, the k_z-projected Fermi surface contours in Fig. 8**b** provided clear evidence of the complex final state, such as the overlapping hole pockets of the sheet C and sheet D hole pockets at X-point in Fig. 9**b**. Moreover, the spectral weight in Figs. 9**c** from Fermi sheet B, manifests as a four-fold background-like projection around the origin in the $X – \Gamma$ direction of the zone boundary overlay. Albeit the L-point hole pocket of Fermi sheet C of Rh is slightly larger than that of theory, our experimental results are in general agreement with the FPLAPW calculations. By ensuring the convergence to the free electron final state model at higher photon energies, Figs. 9**d** and **e** illustrate the selected experimental results obtained at Γ and X-point at 508 eV and 652 eV photon energies, respectively.

7. Conclusions

In this study, we utilized a comprehensive pipeline to experimentally determine high-resolution Fermi surfaces using momentum microscopy for Pd(001) and Rh(001). Our investigation began by thoroughly assessing the viability and limitations of the free electron final state model across a wide range of photon energies. We found that
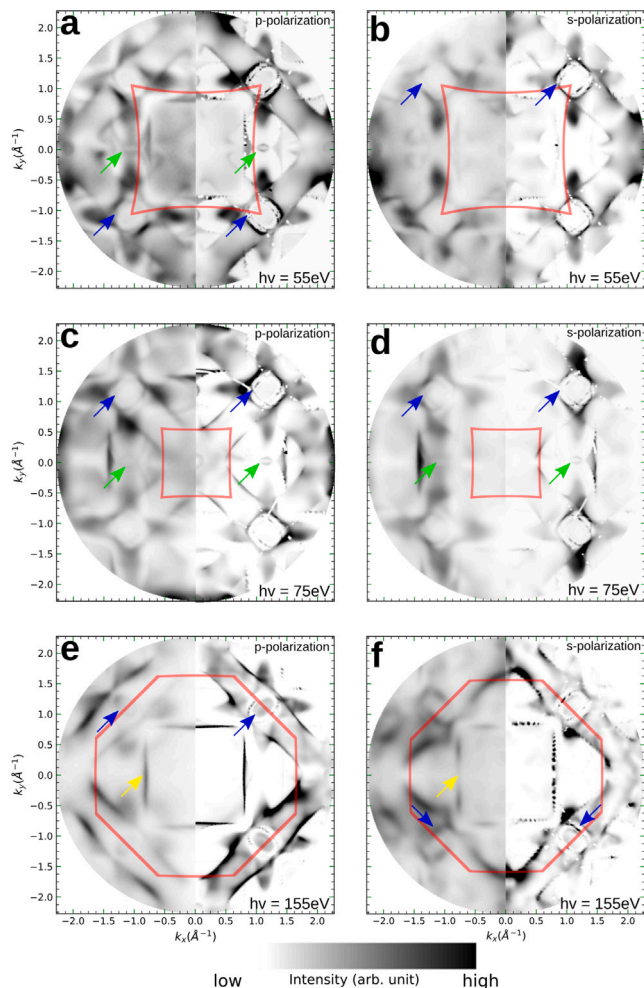
Fig. 7. Experimental photoelectron momentum maps of Fermi surface (left half) and its fully relativistic one-step-model counterpart (right half) for hv = 55 eV (**a-b**), 75 eV (**c-d**) and 155 eV (**e-f**) respectively. Momentum maps (**a**, **c**, **e**) correspond to photoemission geometry of p-polarization whereas momentum maps (**b**, **d**, **f**) correspond to that of s-polarization. The colors of the point of interest (arrows) correspond to the respective color scheme used in Fig. 1**a** and **b**.

the free electron final state model can effectively model the out-of-plane momentum when the free electron wave functions match the final states in the bulk. However, at the boundaries of the bulk Brillouin zone, local band gaps emerge, preventing the penetration of the free electron state into the bulk and leading to the formation of evanescent states.

The presence of evanescent states has two key consequences. Firstly, it results in suppressed intensity at the boundary of the Brillouin zone. The evanescent states prohibit the extension of free electron wave functions into the bulk, thereby reducing the photoemission intensity at these points. Secondly, the evanescent states exhibit a limited lifetime, contributing to a complex-valued self-energy of the final states. This complex self-energy gives rise to the emergence of waterfall-like structures in the photoemission intensities, particularly in the out-of-plane wave vector.

Furthermore, our results emphasize the significance of considering photoemission final-state effects, as we provide a quantitative explanation for satellite structures and ghost states previously attributed to photoemission artifacts. These features can be accurately accounted for

within our theoretical framework by incorporating the complex-valued self-energy of the final states.

We also thoroughly investigated the crossover limits and breakdown of the free electron final state model in both Pd(001) and Rh(001) systems. We discovered that the free electron final state model assumption generally falls apart in a low-energy regime characterized by strong modulation of out-of-plane components, primarily due to the presence of evanescent states. When studying systems of interest, it becomes imperative to consider additional variables such as structural factors, physical interactions, and the information depth, typically represented by the inelastic mean-free-path of photoelectrons.

For instance, in the case of single-crystalline cobalt [38], the convergence towards a free electron-like final state occurs at significantly lower energies. This behavior in cobalt arises from strong electron correlations, which lead to significant band broadening away from the Fermi level. Consequently, even when utilizing a low-energy excitation source, the assumption of a free electron final state model can still be invoked. Thus, the breakdown of the free electron final state model in the low-energy regime highlights the importance of considering system-specific factors, such as electron correlations, to accurately describe the final states in photoemission experiments. These considerations expand our understanding of the limitations and applicability of the free electron final state model in different materials and energy regimes.

Moreover, this experimental study represents a significant advancement as we report the high-resolution Fermi surfaces of Pd and Rh. Specifically, we successfully resolve the long-standing question regarding the existence of an L-hole pocket in the Pd Fermi surface. Our experimentally resolved Fermi surface findings bridge the gap between state-of-the-art theoretical results and experimental observations.

Additionally, the higher valency of Pd leads to a notable shift of the Fermi level towards the band extrema, resulting in the formation of a "jungle gym" like topology characterized by a high density of states. This unique topology suggests the potential for nesting effects across the Pd Fermi surface, as previously discussed [27,39]. These findings provide valuable insights into the intricate relationship between the electronic structure and valency in Pd. However, it is important to acknowledge the limitations of the theoretical models employed in this study. Despite focusing on the Fermi energy, we observe several noticeable discrepancies, such as the size of hole pockets. These deviations underscore the need for more intensive investigations into local and non-local electron correlations in both Pd and Rh systems. By delving deeper into these correlations, we can achieve a more comprehensive understanding of the observed Fermi surface features.

Furthermore, we demonstrate the application of a tomographic technique utilizing an energy-variable light source, enabling the complete resolution of the Fermi surfaces of Pd and Rh. By cross-referencing the calculated Fermi surface features with experimental observations, we establish a robust connection between theory and experiment. This approach provides a powerful tool for studying and characterizing the Fermi surfaces of complex materials.

In summary, our study not only enhances our understanding of the limitations of the free electron final state model and the formation of evanescent states at the boundaries of the 3D Brillouin zone but also provides a quantitative explanation for satellite structures and ghost states. By considering these factors, we improve our understanding of high-resolution Fermi surface tomography and advance the interpretation of photoemission intensities. Additionally, the experimentally resolved high-resolution Fermi surfaces of Pd and Rh underscore the need for further investigations into electron correlations and the limitations of theoretical models. This showcases the potential for bridging theory and experiment in the study of Fermi surfaces, paving the way for future advancements in our understanding of the electronic properties of materials.
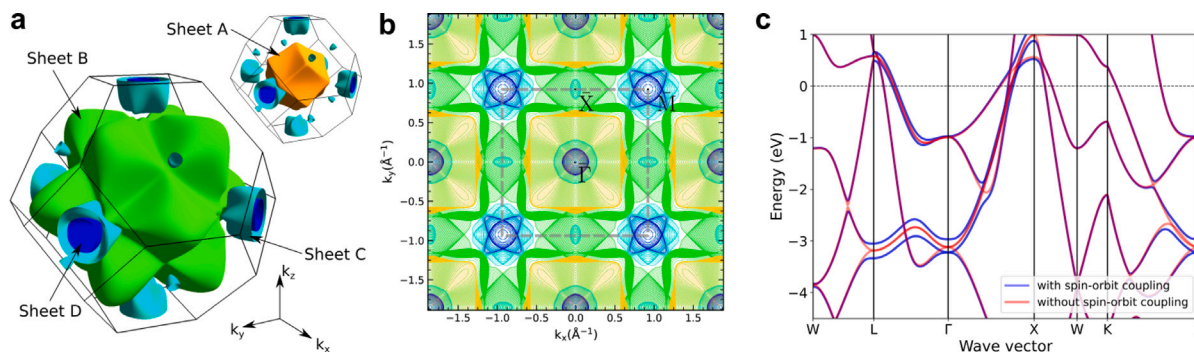
Fig. 8. a Relativistic Fermi surface of Rh calculated using FPLAPW with LDA+U formalism. Inset shows the free electron like Fermi sheet by removing the d-like sheet (green). **b** Projection of the Fermi surface contours of the LDA+U ground state in k_z dimension. **c** Comparison between the ground state calculations with and without consideration of spin–orbit coupling.
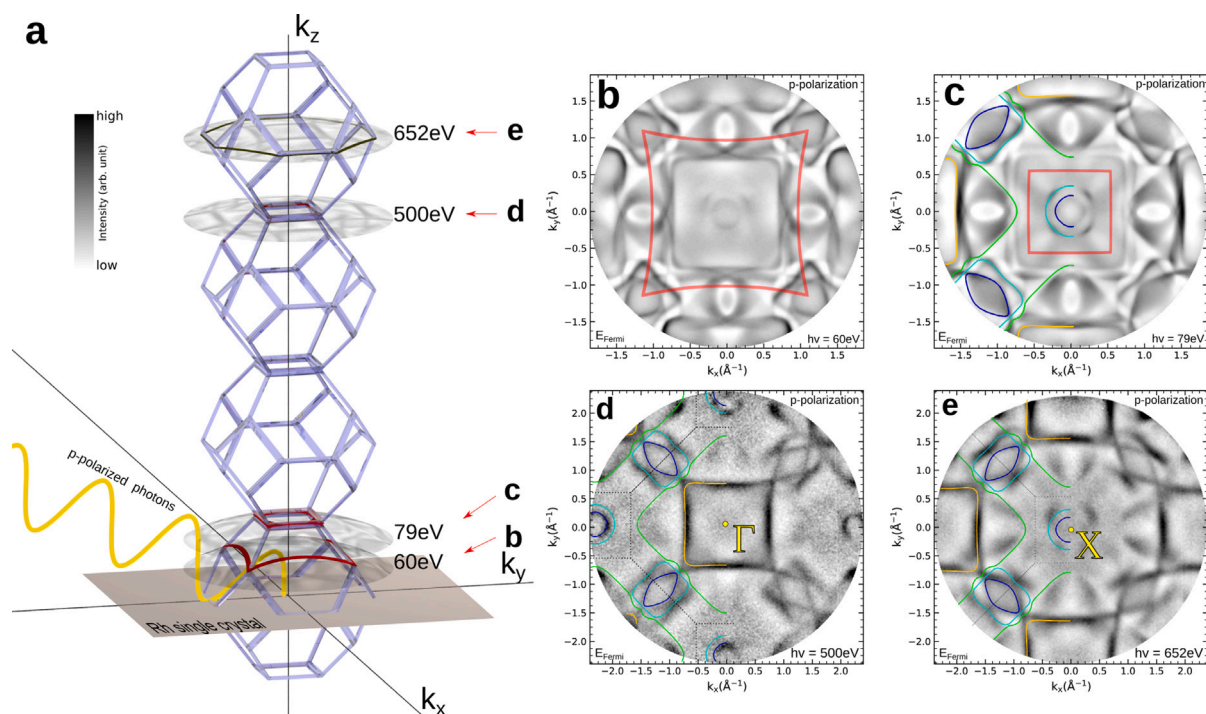
Fig. 9. a Experimental geometry and equi-energy free-electron final state spherical cuts in 3D momentum space corresponding to the experimental momentum maps. **b, c, d, e** show the experimental momentum maps obtained at soft-X-ray energies of 60 eV, 79 eV, 500 eV, and 652 eV, respectively. Red overlay illustrates the intersections between the corresponding momentum disc and the first Brillouin zone boundary in a nearly-free electron final state model whereas the theoretical Fermi contour of palladium from local density approximation is overlaid on the left half of **c, d, e**.

Declaration of competing interest

The authors declare that they have no known competing financial interests or personal relationships that could have appeared to influence the work reported in this paper.

Data availability

Data will be made available on request.

Acknowledgments

Appendix A. Supplementary data

Supplementary material related to this article can be found online at https://doi.org/10.1016/j.ultramic.2023.113820.

References

[1] M.I. Kaganov, I.M. Lifshits, Sov. Phys. Uspekhi 22 (11) (1979) 904–927.
[2] D. Shoenberg, Proc. R. Soc. London. Ser. A. Math. Phys. Sci. 170 (942) (1939) 341–364.
[3] D.H. Dye, S.A. Campbell, G.W. Crabtree, J.B. Ketterson, N.B. Sandesara, J.J. Vuillemin, Phys. Rev. B 23 (2) (1981) 462–473.
[4] J.E. Ortega, F.J. Himpsel, G.J. Mankey, R.F. Willis, Phys. Rev. B 47 (3) (1993) 1540–1552.

[5] P. Grünberg, R. Schreiber, Y. Pang, M.B. Brodsky, H. Sowers, Phys. Rev. Lett. 57 (19) (1986) 2442–2445.

[6] S. Suga, C. Tusche, J. Electron Spectrosc. Relat. Phenom. 200 (2015) 119–142.

[7] S. Hüfner, Photoelectron Spectroscopy, Springer Berlin Heidelberg, 2013.

[8] R. Hora, M. Scheffler, Phys. Rev. B 29 (2) (1984) 692–702.

[9] V.N. Strocov, E.E. Krasovskii, W. Schattke, N. Barrett, H. Berger, D. Schrupp, R. Claessen, Phys. Rev. B 74 (19) (2006) 195125.

[10] H. Ebert, D. Ködderitzsch, J. Minár, Rep. Progr. Phys. 74 (9) (2011) 096501.

[11] J. Minár, S. Mankovsky, J. Braun, H. Ebert, Phys. Rev. B 102 (3) (2020) 035107.

[12] M. Kotsugi, W. Kuch, F. Offi, L.I. Chelaru, J. Kirschner, Rev. Sci. Instrum. 74 (5) (2003) 2754–2758.

[13] C. Tusche, Y.-J. Chen, C.M. Schneider, J. Kirschner, Ultramicroscopy 206 (2019) 112815.

[14] C. Tusche, A. Krasyuk, J. Kirschner, Ultramicroscopy 159 (2015) 520–529.

[15] C. Tusche, M. Ellguth, A.A. Ünal, C.-T. Chiang, A. Winkelmann, A. Krasyuk, M. Hahn, G. Schönhense, J. Kirschner, Appl. Phys. Lett. 99 (3) (2011) 032505.

[16] M. Ellguth, C. Tusche, F. Iga, S. Suga, Phil. Mag. 96 (31) (2016) 3284–3306.

[17] Y.-J. Chen, J.-P. Hanke, M. Hoffmann, G. Bihlmayer, Y. Mokrousov, S. Blügel, C.M. Schneider, C. Tusche, Nature Commun. 13 (1) (2022) 5309.

[18] J. Braun, J. Minár, H. Ebert, Phys. Rep. 740 (2018) 1–34.

[19] C. Kittel, Instructor's Manual to Accompany Introduction to Solid State Physics, Seventh Edition, Charles Kittel, Wiley, New York Chichester, 1996.

[20] W. Sänger, J. Voitländer, Z. Phys. B Condens. Matter 38 (2) (1980) 133–138.

[21] H.C. Jamieson, F.D. Manchester, J. Phys. F: Metal Phys. 2 (2) (1972) 323–336.

[22] V.L. Moruzzi, P.M. Marcus, Phys. Rev. B 39 (1) (1989) 471–474.

[23] G.S. Tripathi, N.E. Brener, J. Callaway, Phys. Rev. B 38 (15) (1988) 10454–10462.

[24] G. Chang, S.-Y. Xu, B.J. Wieder, D.S. Sanchez, S.-M. Huang, I. Belopolski, T.-R. Chang, S. Zhang, A. Bansil, H. Lin, M.Z. Hasan, Phys. Rev. Lett. 119 (20) (2017) 206401.

[25] P.-J. Hsu, J. Kügel, J. Kemmer, F.P. Toldin, T. Mauerer, M. Vogt, F. Assaad, M. Bode, Nature Commun. 7 (1) (2016) 10949.

[26] The Elk code, URL https://elk.sourceforge.io/.

[27] A. Östlin, W.H. Appelt, I.D. Marco, W. Sun, M. Radonjić, M. Sekania, L. Vitos, O. Tjernberg, L. Chioncel, Phys. Rev. B 93 (15) (2016).

[28] D.A. Stewart, New J. Phys. 10 (4) (2008) 043025.

[29] M. Sekania, A. Östlin, W.H. Appelt, S.B. Dugdale, L. Chioncel, Phys. Rev. B 104 (20) (2021).

[30] A. Winkelmann, M. Ellguth, C. Tusche, A.A. Ünal, J. Henk, J. Kirschner, Phys. Rev. B 86 (8) (2012).

[31] J. Schusser, H. Bentmann, M. Ünzelmann, T. Figgemeier, C.-H. Min, S. Moser, J. Neu, T. Siegrist, F. Reinert, Phys. Rev. Lett. 129 (24) (2022) 246404.

[32] A. Locatelli, A. Bianco, D. Cocco, S. Cherifi, S. Heun, M. Marsi, M. Pasqualetto, E. Bauer, J Phys. IV (Proc.) 104 (2003) 99–102.

[33] H. Bentmann, H. Maaß, J. Braun, C. Seibel, K.A. Kokh, O.E. Tereshchenko, S. Schreyeck, K. Brunner, L.W. Molenkamp, K. Miyamoto, M. Arita, K. Shimada, T. Okuda, J. Kirschner, C. Tusche, H. Ebert, J. Minár, F. Reinert, Phys. Rev. B 103 (16) (2021) l161107.

[34] H. Hayashi, K. Shimada, J. Jiang, H. Iwasawa, Y. Aiura, T. Oguchi, H. Namatame, M. Taniguchi, Phys. Rev. B 87 (3) (2013) 035140.

[35] N. Memmel, Surf. Sci. Rep. 32 (3–4) (1998) 91–163.

[36] V. Heine, Proc. Phys. Soc. 81 (2) (1963) 300–310.

[37] S. Kevan (Ed.), Angle-Resolved Photoemission, Elsevier Science & Techn., 1992.

[38] C. Tusche, M. Ellguth, V. Feyer, A. Krasyuk, C. Wiemann, J. Henk, C.M. Schneider, J. Kirschner, Nature Commun. 9 (1) (2018) 3727.

[39] S.B. Dugdale, Phys. Scr. 91 (5) (2016) 053009.